Journal of Materials Chemistry A

ROYAL SOCIETY OF CHEMISTRY

PAPER

Cite this: DOI: 10.1039/d6ta00639f

Decoupled green hydrogen production using platinum-free catalysts in a bicarbonate electrolyte

Luís Pinho, Mark Potter and Kathryn E. Toghill *

Received 22nd January 2026
Accepted 9th June 2026

DOI: 10.1039/d6ta00639f

rsc.li/materials-a

Electrochemical water splitting is crucial for decarbonizing industrial processes and integrating renewable energy. Conventional electrolysers generate H_2 and O_2 simultaneously in neighbouring compartments using critical raw materials (CRM) as catalysts and corrosive electrolytes, posing safety and cost challenges. Decoupled electrolysis addresses this by separating product formation from electrode processes using electrochemically generated redox mediators and highly dispersed catalysts instead of electrodes and heterogeneous two-dimensional interfaces. In this work we demonstrate decoupled electrolysis at near-neutral pH using a bicarbonate buffer and a highly reducing redox mediator, chromium propanediamine tetraacetate. We compared CRM-free electrocatalysts, MoS_2, Mo_2C, Ni, Ni_xS_y, and Ni_xP_y against V10 Pt (Vulcan carbon with 10% Pt loading), with MoS_2 showing the highest faradaic efficiency. We further analyzed hydrogen evolution reaction (HER) kinetics and thermodynamics using open circuit chronopotentiometry (OCCP) and UV-vis spectroscopy to follow mediator discharge with MoS_2. Finally, we compare the performance of a conventional electrolyser with MoS_2 catalysts in bicarbonate with the decoupled approach, and find that the decoupled performance is superior, despite added energy penalty of −0.6 V of Cr reduction compared to HER. This approach offers a safer, CRM-free alternative to conventional water electrolysis and is compatible with renewable energy storage and green electricity integration.

Introduction

Green hydrogen is set to play a key role in the transition to a net zero energy network. In applications for which electrification is not a viable option, the use of green hydrogen as a fuel, feedstock, or reducing agent will be key to enable further decarbonisation of industry and transport. Green hydrogen is a diverse energy vector and can be produced as a means of energy storage and peak load balance, or as a means of replacing other forms of fossil fuel hydrogen in our industrial networks. The hydrogen market is evolving rapidly with uncertainties on how best to utilise the end product.[1] However, one constant driver is to achieve green hydrogen at scale, at low cost, using intermittent energy sources and readily available resources.

Electrolysis is a long-commercialised process through an array of technologies such as proton exchange membrane (PEM) and alkaline water (AWE) electrolysers.[2] Nevertheless, large-scale adoption is still hindered by high cost of electrocatalysts, safety issues (gas crossover and corrosive electrolytes), low efficiency and poor durability.[3] Coupling water electrolysis to renewable energy sources is also difficult due to intermittent supply of renewable electricity.[4] Among the limitations of water electrolysis is the co-production of oxygen on the anode; a commodity with little-to-no value when produced through electrolysis yet is the driver for higher overpotentials and lower yields due to the challenging proton coupled electron transfer kinetics.[5]

An emerging technique in electrochemistry is the use of electrochemically generated charge transfer mediators to drive catalysed reduction and oxidation reactions distinctly away from the electrode interface. This approach allows for a decoupling of the anode and cathode reactions. As such, HER can be performed independently of OER (or another more-valuable reaction). Symes and Cronin introduced time decoupled electrolysis in 2013 as a new approach to water splitting in which the electrochemically generated redox mediator is used to store charge and protons. They used the polyoxometalate (POM) phosphomolybdic acid as an electron-coupled proton buffer to store protons and electrons released during water oxidation (OER) and release them during water reduction (HER).[6] In principle, this concept can be applied to decouple any electrolytic reaction and was further developed in presence of several PGM catalysts.[7]

At a similar time, the Girault group developed the 'dual circuit flow battery', where a vanadium–cerium redox flow battery was adapted to produce hydrogen and oxygen *via* water splitting in a spatially decoupled manner. The redox mediators V(II) and Ce(IV) were generated in an electrochemical charging

Department of Chemistry, Lancaster University, Lancaster, LA1 4YB, UK. E-mail: k.toghill@lancaster.ac.uk

step, followed by chemical discharge over catalytic beds in separate reactors.[8] The positive redox couple was further developed by swapping it with Mn(II)/Mn(III), resulting in a more stable system, with enhanced gas purity and greater efficiency.[9] Decoupling water splitting in this way requires matching of the mediator's redox potential with the desired electrochemical reaction, ensuring there is a thermodynamic driving force to enable the reduction of protons or oxidation of water. It also introduces two more elements: flexibility and safety due to inherent temporal and spatial separation between O_2 and H_2 evolution. More recently, this redox mediated approach has been expanded to alkaline electrolytes using both metal complexes,[10] and aqueous organic redox mediators (Table S1).[11]

Other approaches have been used to specifically decouple water splitting using solid electrodes as redox catalysts for electrolysis only,[12] or combining with energy storage.[13] Recently, these approaches have been developed in near neutral electrolytes.[14]

Water splitting, especially under acidic conditions, still primarily uses platinum group metals (PGM) as electrocatalysts, which is a problem when concerning cost, scale-up and the sustainability of this technology. Alkaline electrolysis notably allows the use of non-PGM catalysts such as nickel. However, the reported demonstrations of decoupled HER (DeHER) in alkaline have to-date relied on modified Pt catalysts.[11] This is in part due to the redox potentials of the mediators being only slightly higher in energy than the thermodynamic requirement for HER, and thus only Pt as the best-in-class catalyst enabled DeHER. In acid, the dual circuit flow battery was demonstrated using molybdenum carbide catalyst to great effect. However, oxygen evolution still depended on iridium or ruthenium catalysts.[8,14]

Other than the recent work of Slobodkin *et al.*,[14] the systems evaluated to date use either highly acidic (pH < 0) or highly alkaline (pH > 14). Of all the candidates we identified for liquid redox mediator in neutral or near neutral pH (Table S2), none of these mediators offers the same electrochemical driving force while remaining accessible through electrolysis without competing HER at less extreme pH values.[15–18] This is relevant to the growing interest in sea water electrolysis, which will require minimal water processing to enable cost-effective electrolysis.[19,20] Water electrolysis at pH values closer to neutral is still being mechanistically explored, as the classic descriptions of rate limiting kinetic steps do not apply.[21] At these pH values, bicarbonate buffer is particularly relevant due to its presence in biological systems and in sea water electrolysis.[22–27]

Our previous work has recently demonstrated that electrochemical CO_2 reduction (ECO_2R), can be decoupled in a similar manner to HER using a highly reducing mediator[28,29] and nano faceted bismuth catalyst.[30] In such systems, the bicarbonate buffer plays a pivotal role due to its ability to regulate pH variations around neutral values; as the pH increases due to the consumption of protons, the speciation of the buffer adjusts. Besides the buffering of acid–base reactions in solution, the carbonate species may play a primary role in the HER mechanism. However, to-date this has only been considered on platinum and gold single crystal electrodes.[22]

Here we aimed to evaluate HER by CRM-free catalysts in a mildly alkaline pH, both conventionally and in a decoupled reaction. By applying a high driving force mediator, we were able to avoid the issue of varying overpotential to ascertain faradaic efficiencies. However, when comparing best in class platinum-free catalyst materials in a conventional electrolyser, we found the decoupled system to be higher performing and more efficient, despite the apparent high overpotential.

Results and discussion

Redox mediator and catalyst characterisation

K[CrPDTA] was synthesised using the procedure previously reported by the Marshak group[28] with very slight adaptations, detailed in the Experimental section. CHNS analysis was used to confirm the composition and stoichiometry of the mediator. It indicates the presence of a small sulphate impurity (2–3%), along with 3 waters of crystallisation. Measured: (6.77% N, 31.02% C, 4.12% H, 0.22% S), expected: (6.26% N, 29.53% C, 4.51% H, 0.00% S). FTIR analysis of the compound (Fig. S1) shows good agreement with previous results,[28] showing the characteristic carbonyl bands at around 3400, 1630 and 1650 and N–H stretching peaks (2930 cm^{-1}) that can all be associated with PDTA.

The crystallographic information file provided in the literature[26] was used to simulate PXRD patterns (Fig. S2). The simulated K[CrPDTA] PXRD patterns obtained show a very good match with the synthesized K[CrPDTA]. In addition, given the small sulphate impurity detected using CHNS elemental analysis, we obtained additional experimental PXRD patterns for $CrK(SO_4)_2 \cdot 12H_2O$ and for K_2SO_4. Small impurities of both compounds could be present in our material, as we observed some overlapping of peaks observed for the synthesized K[CrPDTA] and the intensity maxima obtained for $CrK(SO_4)_2 \cdot 12H_2O$ and for K_2SO_4. Small changes in hydration state could also justify the slight discrepancies between simulated and experimental patterns obtained for K[CrPDTA].

A selection of readily available, CRM-free catalysts powders, known to be HER active in different pH conditions were evaluated in their as-bought condition. Powders of MoS_2, Mo_2C, Ni_xP_y, Ni_xS_y and Ni (from atmospheric plasma spray, APS) were characterised prior to use by XRD and SEM, (Fig. 1, S3 and S4).

The pXRD measurements of Mo_2C and MoS_2 particles present peaks than can be ascribed to the hexagonal β-form[31,32] and the hexagonal 2H-phase[33,34] (Fig. S3), respectively. For the latter, the very high intensity peak at around 15° can be assigned to the [002] plane, which indicates the presence of few-layer MoS_2 nanosheets instead of a bulk structure with longer range order.[33,35]

The Ni-containing pXRD pattern indicates that Ni_xS_y could be a mixture of Ni_3S_2 (heazlewoodite) and Ni_3S_4 (polydimite), while Ni_xP_y, is likely to be a mixture of Ni_2P and Ni_5P_4 [19,34] and possibly $Ni_{12}P_5$.[36] For Ni APS powder, we observe three peaks corresponding to the [111], [200] and [222] planes of the face cubic centred structure of the metal.[37] For comparison, commercial V10Pt was also characterised. This shows a very broad [111] diffraction peak at 40° of the fcc structure of small-

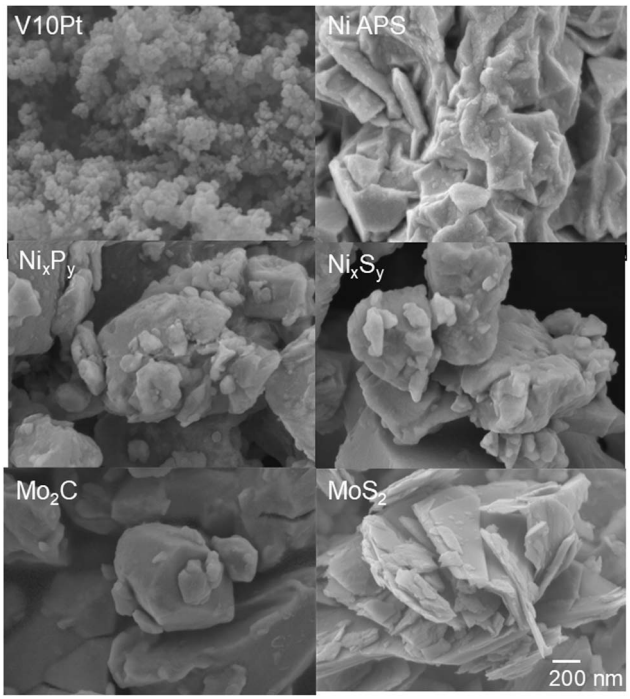

Fig. 1 SEM images obtained for the electrocatalysts under study. Scale bar 200 nm. V10Pt presents the structure of graphitized carbon spheres of about 20 nm size. Ni APS presents agglomerates of 3–7 μm particles, with surface roughness that is clearly visible at a lower magnification. Ni_xP_y and Ni_xS_y consist of larger particles with irregular shape in the range of 1–10 μm. Mo_2C has particle sizes in the range of 1–5 μm. MoS_2 presents the distinctive features of a 2D material, with micron-long platelets oriented along the [002] plane of hexagonal 2H-phase of MoS_2, which are 20–90 nm thick.

size, well-dispersed Pt. The peak at approximately 25° is related to the [002] reflection of amorphous carbon.[38]

SEM images were obtained at two different magnifications to reveal the morphological features of the materials (Fig. 1, S4 and S5). Mo_2C has particle sizes in the range of 1–5 μm.[32] At higher magnification, large bulk particles with a smooth surface can be observed. Ni_xP_y and Ni_xS_y consist of larger particles with irregular shape in the range of 1–10 μm. At higher magnification, a greater number of smaller size particles can be observed, as well as a coarser surface. Ni APS presents agglomerates of 3–7 μm particles, with surface roughness that is clearly visible at a lower magnification. At greater magnification, these surface features consist of 10 nm-thick platelets, as well as numerous smaller particles that are evenly distributed and coarsen the surface. We hypothesize that these features are generated by the atmospheric plasma spraying (APS) manufacturing process. MoS_2 is also manufactured *via* the APS process.[39] Unlike Ni APS, the MoS_2 presents the distinctive features of a 2D material, with micron-long platelets oriented along the [002] plane of hexagonal 2H-phase of MoS_2, which are 20–90 nm thick (Fig. S5). Finally, V10 Pt presents the structure of graphitized carbon spheres of about 20 nm size. These spheres are very well dispersed in a coarse, low-density structure.

Fig. 2a shows an overlay of linear sweep voltammograms obtained for the catalyst materials in bicarbonate buffer. The electrodes were constructed using a carbon paste composite comprising 1/3 active material by weight. All the composite materials containing non-Pt catalyst showed appreciable activity from *ca.* −0.2 to −0.4 V *vs.* RHE depending on the material. Previous benchmarking studies present the values of overpotential required to reach 10 mA cm^{-2} per geometric area as the primary figure of merit for benchmarking HER catalysts.[40] In our case, the smallest overpotential is still observed for V10Pt (208 mV), followed by a group of Ni APS, MoS_2 and Mo_2C (501, 542, and 565 mV, respectively) and another group of Ni_xS_y and Ni_xP_y (603 and 692 mV) (Table S3). The carbon paste response in the absence of any added catalysts materials shows pronounced activity from *ca.* −0.7 V reaching 10 mA cm^{-2} at −0.88 V *vs.* RHE. Thus, the electrocatalytic activity of the materials towards heterogeneous HER in bicarbonate buffer can be considered V10Pt > Ni APS > MoS_2 > Mo_2C > Ni_xS_y > Ni_xP_y.

Electrochemical characterisation

These results are corroborated by earlier studies comparing the electrocatalytic performance of electrocatalysts in seawater containing bicarbonate ions, at near neutral pH, showing metal sulfides and phosphides as materials with the required properties for the HER at near-neutral pH.[19,20] For some of the catalysts under study, we note that a preconditioning process could be taking place in the measurements (V10Pt, Ni APS, Mo_2C, MoS_2).[31,41] V10Pt shows onset more positive than the theoretical thermodynamic conditions for the HER on platinum, a phenomenon previously observed by MacDonald *et al.*[34]

Typically, Ni is an active catalyst in strong hydroxide environments (>0.1 M), corresponding to the formation of catalytic $Ni(OH)_2$ layers. Such layers are not anticipated in the bicarbonate electrolyte. It is therefore surprising that the Ni APS is the second best performing electrocatalyst in the medium. While onset potential appears at −120 mV for the Ni ASP, the potential required to pass a current 10 mA cm^{-2} is very similar to that of the molybdenum catalysts at around −500 mV.

The composite nature of the electrodes and lack of mass transport control prevent any meaningful Tafel analysis from the LSVs. In addition, as previously reported by Koper *et al.*, the presence of bicarbonate in the electrolyte could change the mechanism and the kinetics of the reaction, as it could be acting as a proton donor.[22]

Decoupled HER with CrPDTA in bicarbonate buffer

The fully chelated chromium complex of 1,3 propanediamine-*N*,*N*,*N*′,*N*′-tetraacetic acid (CrPDTA) has recently been highlighted as an aqueous RFB anolyte with an unusually negative single electron reduction at $E^\circ = -1.1$ V *vs.* the standard hydrogen electrode (SHE) (−0.6 V *vs.* RHE in 1 M $KHCO_3$ electrolyte, pH 8.5) (Fig. 2b), along with high solubility (1.2 M) and long-term stability.[28,29] In this heterogeneous DeHER mechanism, the redox-active mediator, Cr(III)PDTA, is first electrochemically reduced in the flow cell (a typical galvanostatic charging profile is shown in Fig. S6, against ferrocyanide

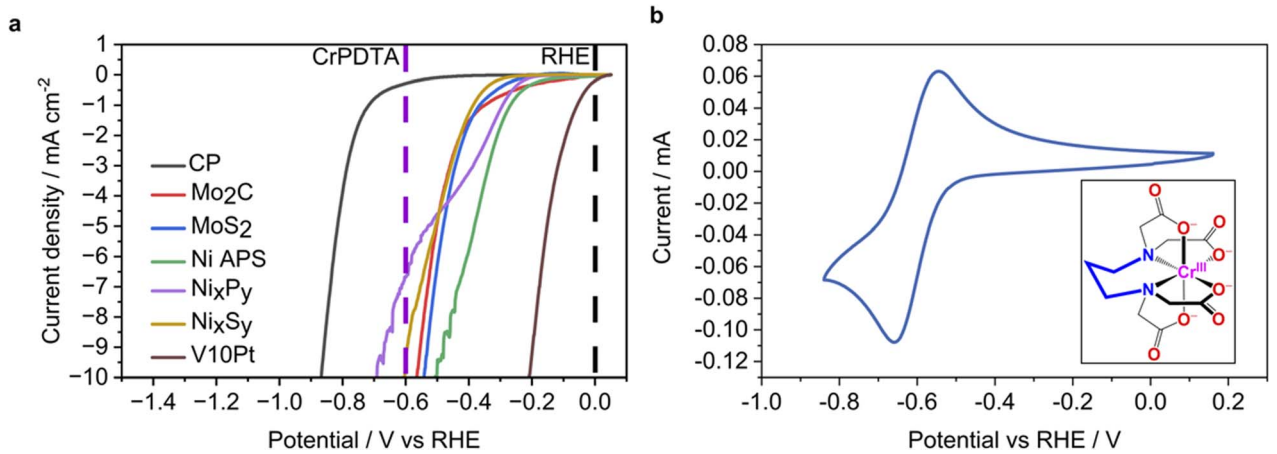

Fig. 2 Linear sweep voltammetry (LSV) of electrocatalysts and cyclic voltammetry of Cr PDTA. (a) LSV obtained for the electrocatalysts under study in aqueous 1 M $KHCO_3$ supporting electrolyte (5 mV s^{-1}) under N_2. Electrodes are all carbon paste composites containing 1 : 2 active material, Ag/AgCl (3 M) reference electrode and Pt counter. The starting current has been normalised to 0 mA cm^{-2} to better review the performances attributed to HER. Dashed lines indicate the equilibrium potentials for the reversible hydrogen electrode (black) and CrPDTA (purple) (b) (main) cyclic voltammograms recorded in 1 M $KHCO_3$ supporting electrolyte in water with) 10 mM Cr PDTA using a glassy-carbon electrode (scan rate of 100 mV s^{-1}). Peak separation of 285 mV with broad peaks indicates a quasi-reversible redox process with slow kinetics. (inset) Chemical structure of Cr(III) PDTA.

oxidation to ferricyanide). Subsequently, an aliquot of the charged Cr(II) mediator is transferred to a separate vessel containing a catalyst, where HER occurs *via* chemical discharge driven by the mediator. Fig. 3 illustrates the overall workflow, including the sequence of electrochemical charging and catalysed chemical discharge steps and corresponding stoichiometry.

The importance of the choice of suitable mediator/catalyst redox pairs cannot be overemphasized: in its reduced form, Cr(II)PDTA can provide sufficient driving force for hydrogen evolution (600 mV) allowing the unhindered evaluation of heterogeneous catalysts with varying onset potentials. The selection of electrocatalyst materials was made on the basis of previous exploration of materials for decoupled water splitting strategies in acidic and in alkaline electrolytes.[8,10,11,34] Regarding CrPDTA, to our knowledge, this is one of very few mediators that is able to operate at these pH values with sufficient (albeit excessive) driving force (Table S2).

Bulk powders of the six materials were screened as HER catalysts using Cr(II)PDTA in a batch process using fully charged mediator to establish total faradaic yield (Fig. S5). The results are given in Fig. 4 following discharge reactions with 5 mL redox mediator and 5 mg of catalyst, completed in triplicate. Using a fixed volume of charged mediator solution at a known

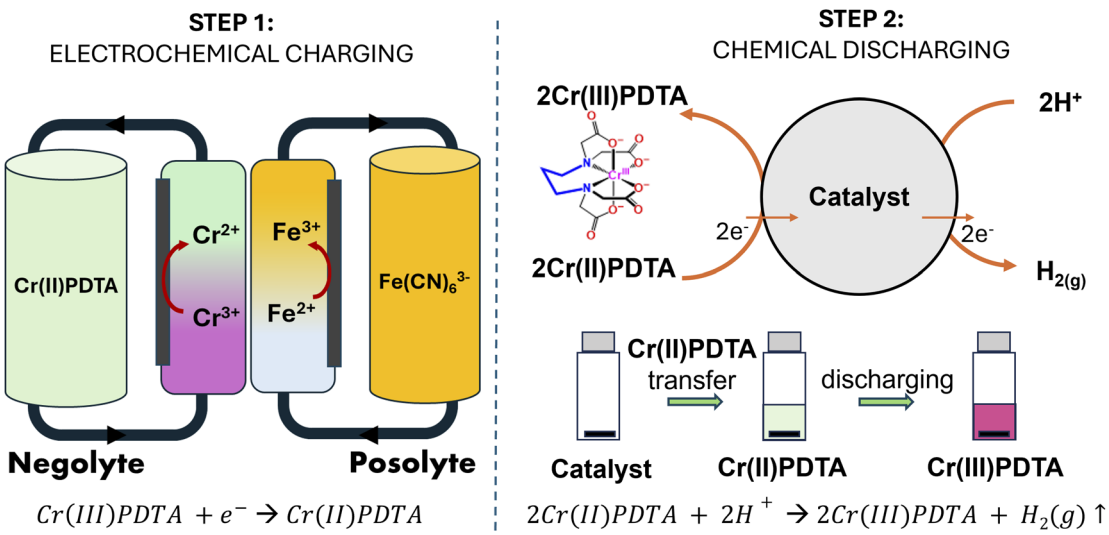

Fig. 3 Simplified protocol of a redox-mediated heterogeneous hydrogen evolution reaction. In step 1 a redox-active species (CrPDTA) is electrochemically reduced using flow battery architecture. In step 2 the reduced mediator, Cr(II), is chemically discharged over a suitable catalyst which transfers electrons to produce hydrogen gas. The result in indirect electrochemical HER.

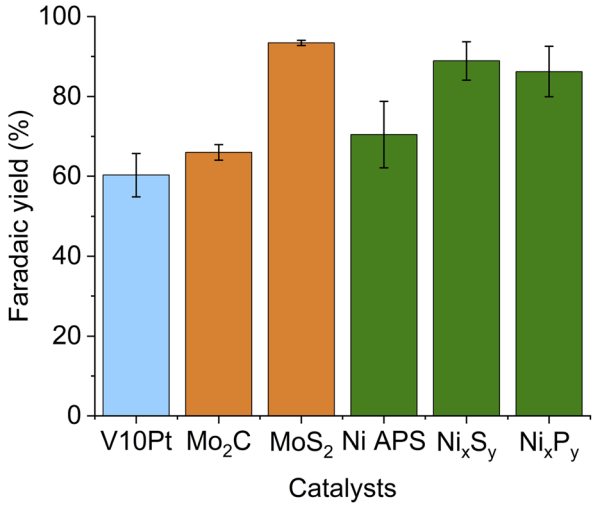

Fig. 4 Faradaic yield for hydrogen with each electrocatalyst under study. Discharge reactions without stirring of the solutions. 5 mg of catalysts in 5 mL of 10 mM CrPDTA. Hydrogen quantified by GC-TCD at end of reaction determined by colour change of mediator.

concentration, the total theoretical charge available for HER is known, allowing for the determination of faradaic yield (FY) as quantified by gas chromatography. These experiments were developed in large batches in order to maximise the number of catalysts and replicates tested. Full conversion was achieved overnight without stirring to avoid mechanical degradation of the magnetic catalysts and to better allow comparison between materials. As such, no kinetic information was determined from this initial screening.

MoS_2 gave the highest hydrogen yield (93.39 $\pm$ 0.66) and notably the most consistent yield with little variation between batches. This material is closely followed by Ni_xS_y and Ni_xP_y (88.89 $\pm$ 4.77 and 86.23 $\pm$ 6.29, respectively) and subsequently Ni APS with the most variable response and average yield of 70.45 $\pm$ 8.35%. Mo_2C gave a consistently low response of 65.98 $\pm$ 1.95%, and quite remarkably, the Pt catalyst used for comparison gave the lowest yield of 60.29 $\pm$ 5.40%. Fig. 2a shows that MoS_2 has the third lowest potential at 10 mA cm^{-2}, achieved at 542 mV, much less negative than the CrPDTA. However, the potentials do not completely correlate to the conversion efficiency of the catalysts, evidence by the low performance of the Pt catalysts in the decoupled reaction. Different dynamics of the reactions and their microkinetic effects may need to be considered to explain their performance. Catalyst-free control reactions indicated that no hydrogen was produced *via* decomposition of the mediator.

Of the highest performing materials, MoS_2 has at least one nanosized dimension (20–90 nm-thick platelets) and a correspondingly high surface area with highly exposed active edge sites.[42] Every other material had a particle size in a range greater by one order of magnitude, and as such had a much lower surface area despite the mass deployed (5 mg for all catalysts). The V10Pt material comprises nanoparticles of Pt on a Vulcan carbon support and may have a substantially lower performance as the active material is just 10% of the 5 mg mass used. Indeed, the LSV data concerns carbon paste electrode composites of the active materials, whereas the bulk studies used the unsupported materials, except for V10Pt. To ensure the lower mass of V10Pt was not the cause of its lesser performance we tested V10Pt in 10-fold mass (50 mg). Conversely, the faradaic yields obtained decreased dramatically to 29.35 $\pm$ 4.17%. A similar increase for MoS_2, also decreased the faradaic yields (Fig. S7).

Spent electrocatalysts were recovered from reaction vessels, washed and dried in air. Only small amounts of sample could be recovered and washed in deionised water. A zero-reflection silicon holder was used to remove any contribution from the stainless steel holder due to small sample thickness. Information for Mo_2C and Ni_xP_y could not be obtained because the amount of these dense catalysts that could be separated from the mixture was too small. Their pXRD patterns are presented in Fig. S8. These catalysts including MoS_2 indicated minimal structural change of the catalyst after the single pass of charged mediator.

Pt is known to be poisoned by CO, and there is a possibility for bicarbonate buffer to spontaneously produce CO_2. In these conditions, there is sufficient driving force from the CrPDTA to reduce CO_2 to two electron products.[30] Typically, in CO_2 reduction reaction, Pt is not evaluated as a catalyst as it would favour the competing HER reaction. However, there is a possibility that the Cr PDTA with Pt reaction is evolving some CO that is subsequently suppressing the Pt activity.

In the recent microkinetic study by Koper *et al.* the mass transfer dynamics were shown to be crucial to the bicarbonate HER reaction on Pt and Au electrodes. The local pH changes would also influence the catalytic reaction, due to concomitant water reduction and dependence on cation identity and specific electrode area.[22] However, in the decoupled scenario the mass transfer dynamics are substantially different with a large buffer effect expected owing to the pseudo-homogeneous process.[30]

As hydroxide ions are an expected product of the HER, and without any balancing oxidation, the pH of the mediator solution will increase when used in a batch reaction. In these conditions, the $KHCO_3$ electrolyte reacts with the hydroxide to buffer the pH. In its fresh state, with 1 M $KHCO_3$ as the supporting electrolyte, the pH was around 8.5. When CrPDTA is added, the pH slightly increases to 9.6. Once spent, the pH remains around 9.3, suggesting the carbonate equilibrium is somewhat able to buffer against pH change.

Carbonate electrolytes effectively increase the activity of aqueous CO_2 and contribute directly to the HER aiding in mass transport to the catalyst surface and providing a buffering effect against localised pH change during electrolysis. For the same pH and cation concentration, Koper *et al.*[22] clearly measure a higher HER current and a less negative onset potential in the presence of bicarbonate buffer compared to a solution containing $NaClO_4$. More recently Baker *et al.*[27] also reported that the proton donor switches from HCO_3^- at low overpotential to H_2O at high overpotential, which strengthens the role of HCO_3^- acting as a donor in our work.

The faradaic yields observed were typically in the 50–95% range, indicating some inefficiency in the unstirred batch

methodology whereby charge is lost to a number of unobserved processes. The first is the reduction of O_2, to which the charged mediator is highly susceptible. Care was taken to ensure the mediator remained under N_2 atmosphere during charging and transfer to a glovebox and vials. Catalytic reactions took place inside the glovebox. However, it is unavoidable that some charge will be lost due contact with O_2 from residual air, which was always observed in the GC analysis. In order to elucidate the source of oxygen in gas analysis, representative gas chromatograms of laboratory air, glovebox atmosphere and 30% H_2 in balance N_2 calibration gas are shown in Fig. S9. We hypothesize that the presence of oxygen in our samples occurs mainly when the septa of our reaction vessels are pierced for gas sample collection and lab air inevitably enters the reactor. It also assumed that the mediator is at a 100% state of charge from the colour change and charging profile, however this is not quantitative. Furthermore, it is possible that gaseous products are lost during sample collection and injection before GC analysis.

A further loss of charge occurs due to the equilibration of the heterogeneous catalyst materials in the electrolyte. This equilibration of a conductor in its local environment is anticipated in the formation of a double layer on the solid surface of the electrocatalyst,[43] and to bring the Fermi level of the catalyst in line with the electrochemical potential of the mediator solution when they are introduced, where the particles effectively behave as a series of redox couples.[44]

It is also known that in capacitive energy storage, ion–electrode interaction strength and cation desolvation have a relevant role in modulating charging mechanisms, offering potential pathways for their optimization. This has relevant implications to our system, as electron transfer occurs between mediator and catalyst, always within a solvation sphere that can be modified to optimize that transfer.[45]

Kinetic studies

As established above, the MoS_2 catalyst produced the highest yield of H_2 out of all those tested. For this reason, it was chosen as a model case for kinetic studies. As Cr PDTA provides considerable driving force over HER, we assume that the change in potential provided by the mediator as it discharges has little influence over the rate of reaction. As such, we can consider only contributions of reduced mediator concentration and catalyst active sites on the rates we measure under different conditions. One notable issue was a large degree of charge transfer from the mediator to the catalyst upon addition that is not necessarily coupled with product formation, which obscures the initial rate of reaction. We consider this to be 'booster like' change transfer, caused by Fermi level equilibration between the mediator and catalyst (Fig. 5a).

Starting with a fixed mediator concentration of 10 mM, the amount of catalyst added was varied between 1 and 15 mg. Open Circuit Chronopotentiometry (OCCP) curves were then obtained providing a voltage change with respect to time (Fig. S10). These were transformed to state of charge (SOC) plots by using calibration curves for known volume ratios of Cr(II)/Cr(III) PDTA (Fig. S11). An example of transforming the OCCP plot to a SOC plot is shown in Fig. S12.

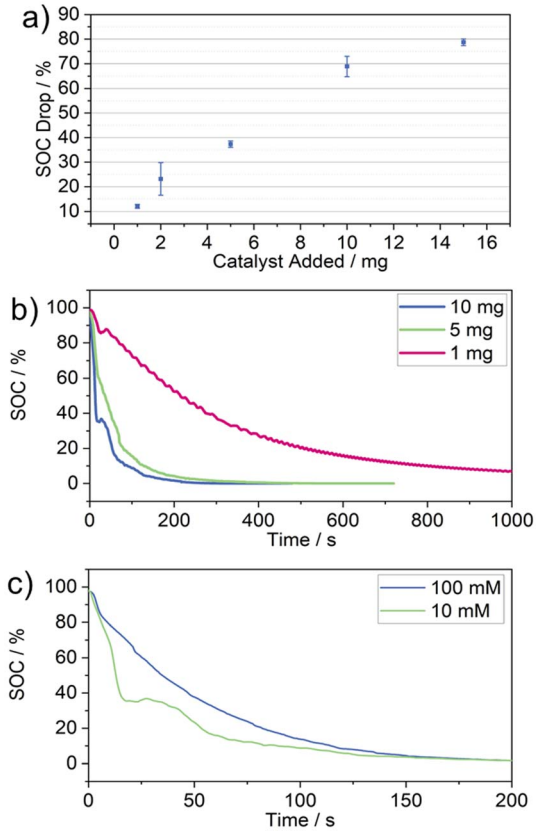

Fig. 5 (a) Graph of initial 'booster like' SOC drop as a function of catalyst mass added for MoS2 catalysed HER mediated by 10 mM Cr PDTA. (b) Graph of SOC *vs.* time for solutions of 10 mM Cr PDTA discharged by 1, 5 and 10 mg of MoS2. (c) Graph of SOC *vs.* time for solutions of 10 and 100 mM Cr PDTA discharged by 10 mg of MoS_2.

The rapid initial charge transfer increased considerably with loading, making initial kinetics difficult to obtain. For the 1 mg addition, we see a small initial drop accounting for about 12% SOC, after which the concentration of reduced mediator falls at a rate indicating first order kinetics. For larger catalyst additions, the initial drop in SOC accounts for too much of the overall charge to accurately examine the rate influence (Fig. 5a and b). However, the system largely still appears to be first order with respect to reduced mediator concentration. Increasing mediator concentration to 0.1 M minimised the impact of this initial charge transfer (Fig. 5c, blue line). As such, the mediator appears first order with respect to the rate in most instances, as was observed for the vanadium mediated case by Reynard and Girault,[9] with the plots of ln([Cr(II)]) *vs.* time appearing most linear for the initial portion of the reaction. Interestingly, the time to 90% discharge was similar for 10 and 100 mM Cr PDTA with 10 mg of MoS_2. This would suggest that even in a stirred regime, mass transport of mediator to the catalyst is primarily limiting the rate even for such a small amount of catalyst.

We repeated the same procedure in absence of the mediator and with insulating, poorly catalytic particles (SiO_2) as a control. After the addition of SiO_2 (Fig. S13), we observe a small oxidation

step of 20 mV, which is smaller than those observed for any of the MoS_2 concentrations. The mediator discharged completely after 5000 s in presence of the lowest concentration of catalyst (1 mg), whereas when SiO_2 is added, complete discharge only occurs after 20 000 s, following a much broader Nernstian curve profile. This shows that the significant changes in potential observed in Fig. 5 are dependent on the ability of MoS_2 to facilitate electron transfer from Cr PDTA to produce hydrogen. In the absence of Cr PDTA mediator (Fig. S14), the variations in potential observed reflect the addition on MoS_2 only.

Further interrogation of the kinetics was performed using water displacement (Fig. S15–S18) to measure the rate at which hydrogen was produced and OCCP (Fig. S15–S18) to track reactant consumption. Herein, we used a fixed mediator concentration with varied amounts of catalyst. The mediator was added to the reactor already containing the catalyst *via* a pressure equilibration funnel, meaning the initial state of charge drop occurs before the circuit is complete and thus the crucial initial SOC drop is not measurable. The method assumes H_2 as the only product. Reliable determination of volume *vs.* time requires a measurable and sufficient volume per second to overcome the induction volume, and as such 10 mM mediator experiments were not attempted.

Utilising 0.1 M mediator, H_2 production tightly followed an exponential curve supporting a first order rate with respect to mediator concentration in good agreement with OCCP measurements. *In situ* OCCP measurement was much noisier than in the dedicated experiment, and as such gave data that was harder to track. In addition, the $E^{0\prime}$ determined from 50% SOC was much more variable with these electrodes, reducing confidence in the SOC calculated from OCP. A comparison of the first 10 seconds of H_2 production for the two catalyst loadings determined initial production rates of 22.8 mL g^{-1} s^{-1} for 25 mg (Fig. S15a) and 13.8 mL g^{-1} s^{-1} for 50 mg (Fig. S16a and Table S4), however as the reaction was found to be first order, these rates do not offer meaningful comparison. Instead, by taking the k_{app} from the exponential fitting applied to the initial rate of H_2 production, we measure 0.00724 ± 0.000469 s^{-1} for 25 mg loading (Fig. S15b) and 0.0131 ± 0.000971 s^{-1} for 50 mg catalyst loading (Fig. S16b and Table S5). Given the 2× increase in catalyst mass, a 1.81× increase in rate was observed, however a relatively large error was observed within each set, with highest and lowest values ranging from 1.41× to 2.51× increases in rate. From this, we reasonably estimate that the catalyst loading also has a first order effect on rate, in line with previously reported results.[8]

To quantify the changes in colour, UV/vis spectra of the mediator were taken for the range of observed states. In its fresh red state, the mediator solution exhibits two strong absorption peaks centred around 510 and 386 nm, with molar absorption coefficients of 116 M^{-1} cm^{-1} and 91 M^{-1} cm^{-1} respectively. Once charged, the green state displays a broad absorbance peak around 665 nm with an absorption coefficient of just 12.4 M^{-1} cm^{-1}. When the mediator contacts the MoS_2 a significant colour change is observed after 30 s, achieving complete discharge by 180 seconds (Fig. S19a) Full mediator reversibility over 2 cycles was also confirmed (Fig. S19b and c).

Conventional electrolyser *vs.* mediator generation and DeHER

To determine the efficiency of the process compared to direct water splitting, an electrolysis cell utilising MoS_2 as a HER catalyst was constructed from carbon cloth spray coated with MoS_2 dispersion. Polarisation curves were taken in both potential controlled (*I–V*) and current controlled (*V–I*) regimes, and galvanostatic electrolysis was performed. This was compared to the same experiments performed on a flow battery with Cr PDTA concentration of 0.1 M, as used in the scaled water displacement system (described in the SI). All experiments were operated against the oxidation of excess ferrocyanide as a counter reaction.

The recorded potential–current curves in Fig. 6 show the potential required to permit a given current in the battery and electrolyser. At very low current density (<10 mA cm^{-2}), the electrolyser operates at a lower potential than the battery, however at current densities above this, the electrolyser becomes increasingly less efficient than the battery. The gradient of the electrolyser demonstrates a higher ohmic resistance in the absence of the redox mediator, despite iR correction being applied. This suggests favourable energy performance from a decoupled system compared to conventional electrolyser at high current densities.

Conventional galvanostatic bulk electrolysis, performed at current densities of 9.375 and 18.75 mA cm^{-2} for 30 minutes, resulted in H_2 yields of 30.5 mL (FE = 94%) and 61.0 mL (FE = 98%) respectively as determined by water displacement measurements. Average operating potentials for the two current densities were 1.732 and 1.778 V. In the 16 cm^2 cell, these current densities correspond to hydrogen production rates of 1.12 and 2.24 mL min^{-1}, as controlled by the fixed current. For the DeHER, the rate of reaction is dependent on both the mediator concentration and the catalyst loading and thus cannot be fixed in the same way. However, the water displacement experiment using 50 mg of MoS_2 catalyst produced hydrogen at an initial rate of 40 mL min^{-1}, with complete discharge occurring at an average rate of 14 mL min^{-1}. Cr PDTA charging at equivalent current densities only required average potentials of 1.633 and 1.704 V respectively.

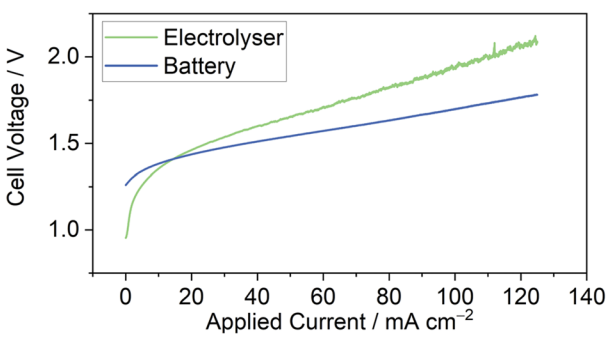

Fig. 6 IR corrected potential–current curves of MoS_2 catalysed HER and Cr PDTA reduction on graphite felt (0.1 M), both against $K_4Fe(CN)_6$ oxidation in a two-electrode flow cell with 16 cm^2 geometric electrode area. Ohmic resistance was measured by PEIS, and was found to be 200 mΩ for the battery and 400 mΩ for the electrolyser.

Another metric for comparison could be coulombic efficiency of charge/product formation, which would indicate a 'decoupling efficiency' in the system. Through the kinetic measurements we have obtained within this work, we determined that the primary factor limiting rate of H_2 evolution during DeHER for a given amount of catalyst is the concentration of the mediator in its reduced state.

We further investigated inefficiencies during charging (and therefore, in the 'decoupling efficiency') by evaluating conversion at a lower state of charge (70% SOC). We used two methods: (1) mixing 100% SOC mediator and 0% SOC mediator to yield a 70% SOC mixture (2) aiming at theoretical 70% SOC by time limited galvanostatic charging. Using these two electrolytes we repeated our decoupled conversion process with 5 mg MoS_2 and report the results in Table S5.

The volumetric mixing method saw 89% of the available charge being converted to product, more or less inline with the yield obtained from using 100% SOC as reported earlier. However, the charge limited charging method resulted in only 80% of the expected yield. It would thus appear there is additional inefficiency in the charging step, which we had avoided previously by intentionally overcharging the mediator solution to ensure 100% SOC. This loss was unanticipated, as previous reports indicated a high coulombic efficiency of charging when operated as a flow battery. This would indicate a further loss of charge efficiency of around 10% from 'decoupling efficiency'.

Determining this true measure of 'decoupling efficiency' is complicated by many factors. First, the charging efficiency of the mediator has been well reported by Marshak *et al.* for use in redox flow batteries, where they commonly report coulombic efficiency above 99.5% when charging up to 90%, albeit at a higher pH which helps to further supress competing HER.

In our case, when comparing the decoupled process to an electrolyser, we chose to consider the voltage efficiency as the most important comparison, rather than the faradaic yields. In our calculations of faradaic yield in the decoupled experiments, we convert the Cr(II) PDTA concentration to moles and relate the available charge of a fully charged solution to moles of hydrogen. For the electrolyser (HER over MoS_2 *vs.* ferrocyanide), the charge passed *vs.* volume produced was compared. For its efficiency, we observed the voltaic efficiency with respect to hydrogen production. As mentioned above, we did not control the end point of charging for our experiments, choosing to overcharge the solution and ensure maximum Cr(II) was available.

From this, we assume that the rate of H_2 production from a decoupled system will be dependent on the rate at which Cr PDTA can be charged, and as it is charged with greater energy efficiency than direct water electrolysis at current densities above 10 mA cm^{-2}, the decoupled system competes favourably with conventional electrolysis.

Conclusions

This work explores an emerging decoupled approach to green hydrogen production (DeHER) demonstrating its operation in bicarbonate buffer at a near neutral pH for the first time. Notably, the catalysts selected and optimised for the system were CRM free to strive for sustainable green hydrogen production. Of the materials tested the highest faradaic efficiency was obtained using MoS_2, achieving 93.4%.

A model, non-potential limiting mediator of Cr PDTA was used to provide a significant driving force for DeHER. While this reduces energy efficiency compared to many previously reported mediators, it allows for a fair comparison of a range of materials without the influence of varying onset potentials, at least as much is reasonably possible in the decoupled system. Further, this high overpotential gives a high degree of confidence that the faradaic efficiencies observed are a result of differences in the materials rather than being due to the range of potential provided by the mediator during the majority of its discharge.

OCCP as a measure of reactant consumption and water displacement as a measure of product formation both indicated first order kinetics with respect to the concentration of reduced mediator when using MoS_2 catalyst, as reported for similar systems. Varying catalyst loading also loosely indicated a first order dependence on catalyst mass, albeit with considerable variation between experiments.

Additional comparison between an MoS_2 electrolyser and Cr PDTA cell, both against $Fe(II)CN_6$, indicated superior energy performance at current densities above 10 mA cm^{-2} for the Cr PDTA cell. This is despite the very negative reduction potential of Cr PDTA at −0.6 V *vs.* RHE. As decoupled HER is very fast, the decoupled process would allow for hydrogen to be produced at lower potential for a given rate than in direct HER using MoS_2 in 1 M $KHCO_3$ electrolyte.

Experimental

Chemicals and reagents

All chemicals were used as purchased without further purification. Chromium potassium sulfate dodecahydrate, potassium hydroxide (≥85%), potassium hydrogen carbonate (99.7%), potassium ferrocyanide (99%), acetone (99%), nickel powder (APS, atmospheric plasma spraying, 99.9% 3–7 micron), nickel sulfide (99.9%) and nickel phosphide (98%) were purchased from Thermo Fisher Scientific (Alfa Aesar, Acros Organics). 1,3-Propanediamine-*N*,*N*,*N*′,*N*′-tetraacetic acid (99%), molybdenum disulfide (APS, 99%), molybdenum carbide (99.5%) and platinized Vulcan (V10, 10% weight loading) were purchased from Merck (Sigma Aldrich). Silica was purchased from VWR and isopropanol (99.5%) from Honeywell. Carbon paste was purchased from IJ Cambria.

Synthesis

Potassium chromium 1,3-propanediamine-*N*,*N*,*N*′,*N*′-tetraacetate (CrPDTA) was synthesised in a single step reaction[28] from readily available precursors. 1,3-Propanediamine-*N*,*N*,*N*′,*N*′-tetraacetic acid (9.18 g) and potassium chromium sulphate dodecahydrate (14.48 g) were added to a round bottom flask (RBF) along with water (60 mL), and the mixture was refluxed for 2 hours. Potassium hydroxide (6 g) was added and the mixture was stirred for a further hour, followed by dropwise

addition of potassium hydroxide solution (5 M) until the mixture was fully neutralised. An equal volume of acetone (approx. 100 mL) was then added, causing a pale purple precipitate to form, which was removed by vacuum filtration. The filtrate was reduced under vacuum to approx. 60 mL and then added dropwise by pipette to ice cold isopropanol (300 mL), resulting in a pink precipitate that was collected by vacuum filtration and washed with isopropanol. CHNS elemental analysis indicated the presence of a small sulphate impurity (2–3%), along with 3 waters of crystallisation.

Measured: (6.77% N, 31.02% C, 4.12% H, 0.22% S), expected: (6.26% N, 29.53% C, 4.51% H, 0.00% S).

Catalyst characterization

Detailed microstructural features of the catalysts materials were examined by Scanning Electron Microscopy (SEM) using a JEOL JSM-7800F (Field Emission SEM, FE-SEM) fitted with an EDX system (X-Max50, Oxford Instruments, Abingdon, UK) at 10 mm working distance and 10 kV voltage. The images were recorded in secondary electron (SE) mode.

X-ray diffraction (XRD) patterns of samples loaded onto glass sample holders were recorded. The samples were mounted on a Rigaku SmartLab 9 kW diffractometer equipped with a germanium (Ge) (220) 2-bounce monochromator using a parallel beam geometry, and a D/teX 250 Ultra 1D detector. The samples were analysed by a $\theta/2\text{-}\theta$ scan with a step size of 0.01°, and a scanning rate of 1° min^{-1}.

Electrode preparation

Carbon paste electrodes (CPE) were prepared by manually mixing graphite-based carbon paste with as-bought electrocatalyst powders in a catalyst to carbon paste ratio of 1 : 2 (20 mg catalyst powder with 40 mg commercial carbon paste). An amount of the mixture was then pressed to fill the empty body of a commercial electrode and polished against the surface of smooth plastic sheet, to give the carbon paste electrode. Note that each CPE did not contain the full 20 mg of catalyst. The electrode consists of a PEEK tube with a back contact made of brass, with a surface diameter of 1.6 mm. Between experiments, the internal surface of the CPE was cleaned using a disposable textured paper brush.

Electrochemical methods

Electrochemical experiments were performed using a Biologic SP300 potentiostat. Voltammetric characterisation was performed in a standard three-electrode cell using a 3 mm diameter glassy carbon disk working electrode, Pt coil counter electrode, an Ag/AgCl reference electrode and a 1 M $KHCO_3$ aqueous solution. Cyclic voltammetry was performed at a scan rate of 100 mV s^{-1} unless otherwise stated. Linear sweep voltammetry was performed at a scan rate of 5 mV s^{-1} with no stirring and 85% iR compensation enabled. The overpotential values used for the HER were corrected according to the following equation:

$$E_{RHE} = E_{Ag/AgCl} + 0.197 + 0.059 \times pH \ (pH = 8.5).$$

Charging of Cr PDTA solutions (10 mM or 0.1 M Cr PDTA, 1 M $KHCO_3$) was conducted galvanostatically in a custom flow cell with a geometric electrode surface area of 16 cm^2, utilising GFD 4.6 SIGRACELL graphite felt electrodes which had been heat-treated for 4 hours at 500 °C under air to improve hydrophilicity, and a Fumapem® F-930 cation exchange membrane (Fumatech GmbH) (Further details in the SI). The redox mediator solution was charged in the custom flow cell against an excess of $K_4[Fe(CN)_6]$ under an inert N_2 atmosphere. Once charged, the solution was transferred to a nitrogen glovebox (Saffron Scientific Ltd).

Direct water electrolysis experiments were carried out by assembling a cell by sandwiching two pieces of carbon felt as the cathode and anode. The active area of the electrode was 16 cm^2. The membrane electrode assemblies (MEAs) were prepared according to a catalyst-coated substrate (CCS) method. The cathode was obtained by dispersing the MoS_2-based catalysts with 28% wt. of Nafion® ionomer in ethanol, followed by further sonication to obtain an ink. The ink obtained was applied onto a carbon paper gas diffusion layer (GDL, 39BB, SIGRACET) using a spray-coating technique with an airbrush, achieving a catalyst loading of 0.86 $mg.cm^{-2}$. On the anode side, a GFD 4.6 SIGRACELL graphite felt electrode which had been heat-treated for 4 hours at 500 °C under air to improve hydrophilicity was used. The two electrodes were separated by a Fumapem® F-930 cation exchange membrane (Fumatech GmbH). The voltage profiles of the flow cell were recorded in galvanostatic and potentiostatic mode. The redox mediator solution was charged in the custom flow cell against an excess of $K_4[Fe(CN)_6]$ under an inert N_2 atmosphere.

Gases that are produced in the tank were collected by water displacement. A measuring cylinder filled with water was placed upside-down in a water bath. The gas produced in the tank was fed into the water-filled measuring cylinder through a silicone tube. The gas production was then determined by the volume of displaced water.

Catalyst testing

Batch decoupled reduction reactions were performed in septum-sealed 20 mL gas chromatography vials. Catalyst powders were placed in uncapped septum-sealed flasks before being introduced in a glovebox so that HER could develop in inert conditions. 5 mL of the charged mediator were introduced in the flasks for HER to occur. They were then capped and left to react without stirring until completeness. The reaction was considered complete when the colour of the mediator solution returned to its discharged state (red).

Gas quantification and product analysis

Gaseous products were analysed by gas chromatography (GC). GC was performed utilising a Shimadzu 2030 equipped with a thermal conductivity detector (TCD) and a ResTek Shin Carbon ST 80/100 column. A calibration curve was obtained for H_2 in the 0–300,000 ppm range, by use of a 30% H_2 (N_2 balance) calibration gas supplied by BOC Ltd, diluted to achieve a range

of concentrations (Fig. S20). Samples were extracted from the headspace of septum-sealed flasks and introduced *via* a gas tight syringe (volume 1 mL VICI® precision Sampling Ltd), in the split/splitless inlet of the gas chromatographer. Calculations for faradaic yield are given in the SI.

Kinetic evaluation

The kinetic performance of CrPDTA mediated catalysis was explored using MoS_2 as a HER catalyst. A solution of 10 mM CrPDTA with 1 M $KHCO_3$ was charged in the flow cell at 100 mA. The charged green solution was kept under nitrogen (N_2) for further use. Aqueous dispersions of MoS_2 90 nm APS were prepared and saturated with N_2. To investigate the effect of the presence of a conductive catalyst *vs.* an insulator, we tested a dispersion of SiO_2 as a control. 1 M $KHCO_3$ and H_2O were also tested as electrolytes in order to isolate the effects produced by the CrPDTA redox mediator. A 20 mL electrochemical cell with glassy carbon working electrode and an Ag/AgCl reference electrode was assembled. To this, 10 mL of mediator were added under magnetic stirring (500 rpm with a small size magnetic stirrer bar) for the establishment of the initial values of open circuit potential. 1 mL of catalyst dispersion was then added after 2–5 minutes of stable measurement. Open circuit chronopotentiometry (OCCP) measurements were then taken continuously until full discharge. The glassy carbon electrode was polished between experiments and the electrochemical cells were cleaned in aqua regia solution to ensure complete removal of the catalyst. All experiments were conducted at least 3 times to ensure reproducibility.

Water displacement experiments were performed in a sealed three-necked round bottom flask, with mediator added from a pressure equilibrating funnel. The gas volumes produced was determined by continuously measuring the mass of water pushed out of an inverted measuring cylinder using a Shimadzu TX2202L series balance, introduced *via* a needle and septum. The method was adapted from a reported procedure,[46] with a custom beaker setup designed to minimise exposed water surface area, reducing induction volume due to surface tension. Simultaneous OCCP measurement was obtained using a graphite rod working electrode and leak-free Ag/AgCl reference electrode (Innovative Instruments Ltd).

UV-visible spectrophotometry was conducted on a Cary 60 UV-vis (Agilent Technologies). Measurements were taken by fully charging a volume of CrPDTA transferring to a nitrogen glove box. The discharge reaction was initiated with 40 mL of CrPDTA and a concentration of 5 mg mL^{-1} of catalyst under stirring, and at regular intervals 5 mL aliquots of the CrPDTA solution were transferred to septum sealed quartz cuvettes using a filter syringe (0.2 μm Nylon filter, Brand). These were then evaluated by UV/vis measurement.

Author contributions

L. P., M. P. and K. E. T. conceptualised the project. L. P. and M. P. synthesised the materials. L. P. and M. P. performed the experiments and analysed the results, with assistance from K. E. T. in methodology. All authors wrote the manuscript and contributed to revision. K. E. T. provided supervision and obtained funding.

Conflicts of interest

There are no conflicts to declare.

Data availability

Data for this article, including raw electrochemical data, gas chromatography, material characterisation data and data processing files are available at Zenodo at https://doi.org/10.5281/zenodo.18342874.

Supplementary information (SI) is available. See DOI: https://doi.org/10.1039/d6ta00639f.

Acknowledgements

The authors are grateful to the European Innovation Council (EIC) under the Pathfinder programme [project number 101070788—DualFlow], UK Research and Innovation (UKRI) under the UK government's Horizon Europe funding guarantee [grant number 10040374]. The authors greatly acknowledge the assistance from Dr Nathan Halcovitch (Department of Chemistry, Lancaster University) with XRD and Elemental analysis, and from Dr Sara Baldock (Department of Chemistry, Lancaster University) with SEM imaging.

References

1 IEA, *Global Hydrogen Review*, 2025, https://www.iea.org/reports/global-hydrogen-review-2025.
2 S. A. Grigoriev, V. N. Fateev, D. G. Bessarabov and P. Millet, *Int. J. Hydrogen Energy*, 2020, **45**, 26036–26058.
3 S. Shiva Kumar and H. Lim, *Energy Rep.*, 2022, **8**, 13793–13813.
4 E. Wallnöfer-Ogris, I. Grimmer, B. Loder, S. Sturm, M. Macherhammer and A. Trattner, *Int. J. Hydrogen Energy*, 2024, **110**, 773–786.
5 J. Li and H. Duan, *Chem*, 2024, **10**, 3008–3039.
6 D. M. Symes and L. Cronin, *Nat. Chem.*, 2013, **5**, 403–409.
7 B. Rausch, M. D. Symes, G. Chisholm and L. Cronin, *Science*, 2014, **345**, 1326–1330.
8 V. Amstutz, E. K. Toghill, F. Powlesland, H. Vrubel, C. Comninellis, X. Hu and H. H. Girault, *Energy Environ. Sci.*, 2014, **7**, 2350–2358.
9 D. Reynard and H. Girault, *Cell Rep. Phys. Sci.*, 2021, **2**, 100556.
10 Y. Ji, F. Zhang, M. Zhou, J. Yu and Q. Wang, *Int. J. Hydrogen Energy*, 2020, **45**, 18888–18894.
11 F. Zhang, H. Zhang, M. Salla, N. Qin, M. Gao, Y. Ji, S. Huang, S. Wu, R. Zhang, Z. Lu and Q. Wang, *J. Am. Chem. Soc.*, 2021, **143**, 223–231.
12 A. Landman, H. Dotan, G. E. Shter, M. Wullenkord, A. Houaijia, A. Maljusch, G. S. Grader and A. Rothschild, *Nat. Mater.*, 2017, **16**, 646–651.

13 B. M. H. Weninger and F. M. Mulder, *ACS Energy Lett.*, 2019, **4**, 567–571.
14 I. Slobodkin, E. Davydova, M. Sananis, A. Breytus and A. Rothschild, *Nat. Mater.*, 2024, **23**, 398–405.
15 T. Liu, X. Wei, Z. Nie, V. Sprenkle and W. Wang, *Adv. Energy Mater.*, 2016, **6**, 1501449.
16 E. S. Beh, D. D. Porcellinis, R. L. Gracia, K. T. Xia, R. G. Gordon and M. J. Aziz, *ACS Energy Lett.*, 2017, **13**, 2.
17 W. Ruan, J. Mao, S. Yang, C. Shi, G. Jia and Q. Chen, *Chem. Commun.*, 2020, **56**, 3171–3174.
18 S. E. Waters, C. M. Davis, J. R. Thurston and M. P. Marshak, *J. American Chem. Soc.*, 2022, **21**, 144.
19 Y. Huang, L. Hu, R. Liu, Y. Hu, T. Xiong, W. Qiu, M. S. Balogun, A. Pan and Y. Tong, *Appl. Catal., B*, 2019, **251**, 181–194.
20 X. Lu, J. Pan, E. Lovell, T. H. Tan, Y. H. Ng and R. Amal, *Energy Environ. Sci.*, 2018, **11**, 1898–1910.
21 Z. Zhou, Z. Pei, L. Wei, S. Zhao, X. Jian and Y. Chen, *Energy Environ. Sci.*, 2020, **13**, 3185–3206.
22 G. Marcandalli, K. Boterman and M. T. M. Koper, *J. Catal.*, 2022, **405**, 346–354.
23 G. Marcandalli, A. Goyal and M. T. M. Koper, *ACS Catal.*, 2021, **11**, 4936–4945.
24 H. Ooka, M. C. Figueiredo and M. T. M. Koper, *Langmuir*, 2017, **33**, 9307–9313.
25 A. Goyal, G. Marcandalli, V. A. Mints and M. T. M. Koper, *J. Am. Chem. Soc.*, 2020, **142**, 4154–4161.
26 J. Zhang, C. Zhang, M. Wang, Y. Mao, B. Wu, Q. Yang, B. Wang, Z. Mi, M. Zhang, N. Ling, W. R. Leow, Z. Wang and Y. Lum, *Nat. Chem.*, 2025, **17**, 334–343.
27 G.-H. Deng, Q. Zhu, J. Rebstock, T. Neves-Garcia and L. R. Baker, *Chem. Sci.*, 2023, **14**, 4523–4531.
28 S. E. Waters, B. H. Robb, S. J. Scappaticci, J. D. Saraidaridis and M. P. Marshak, *Inorg. Chem.*, 2022, 61.
29 B. H. Robb, J. M. Farrell and M. P. Marshak, *Joule*, 2019, **3**, 2503–2512.
30 M. Potter, D. E. Smith, C. G. Armstrong and K. E. Toghill, *EES Catal.*, 2024, **2**, 379–388.
31 H. Vrubel and X. Hu, *Angew. Chem., Int. Ed.*, 2012, **51**, 12703–12706.
32 M. D. Scanlon, X. Bian, H. Vrubel, V. Amstutz, K. Schenk, X. Hu, B. Liu and H. H. Girault, *Phys. Chem. Chem. Phys.*, 2013, **15**, 2847–2857.
33 J. Deng, H. Li, S. Wang, D. Ding, M. Chen, C. Liu, Z. Tian, K. S. Novoselov, C. Ma, D. Deng and X. Bao, *Nat. Commun.*, 2017, (8), 1–8.
34 L. MacDonald, J. C. McGlynn, N. Irvine, I. Alshibane, L. G. Bloor, B. Rausch, J. S. J. Hargreaves and L. Cronin, *Sustain. Energy Fuels*, 2017, **1**, 1782–1787.
35 S. Sathiyan, H. Ahmad, W. Y. Chong, S. H. Lee and S. Sivabalan, *IEEE Photonics J.*, 2015, **7**, 6100610.
36 Y. Wang, X. Feng, S. Yang, L. Xiao and W. Wu, *J. Nanopart. Res.*, 2020, **22**, 1–14.
37 M. Nosan, D. Strmčnik, V. Brusko, M. Kirsanova, M. Finšgar, A. M. Dimiev and B. Genorio, *Sustain. Energy Fuels*, 2023, **7**, 2270–2278.
38 V. S. Pinheiro, F. M. Souza, T. C. Gentil, P. Böhnstedt, E. C. Paz, L. S. Parreira, P. Hammer, B. L. Batista and M. C. Santos, *ChemElectroChem*, 2019, **6**, 5124–5135.
39 X. Wu, A. Piñeiro-García, M. Rafei, N. Boulanger, E. J. Canto-Aguilar and E. Gracia-Espino, *Phys. Chem. Chem. Phys.*, 2023, **25**, 20794–20807.
40 C. C. L. McCrory, S. Jung, I. M. Ferrer, S. M. Chatman, J. C. Peters and T. F. Jaramillo, *J. Am. Chem. Soc.*, 2015, **137**, 4347–4357.
41 H. Vrubel, D. Merki and X. Hu, *Energy Environ. Sci.*, 2012, **5**, 6136–6144.
42 T. F. Jaramillo, K. P. Jørgensen, J. Bonde, J. H. Nielsen, S. Horch and I. Chorkendorff, *Science*, 2007, **317**, 100–102.
43 S. Lin, L. Xu, A. Chi Wang and Z. L. Wang, *Nat. Commun.*, 2020, **11**, 1–8.
44 M. D. Scanlon, P. Peljo, M. A. Méndez, E. Smirnov and H. H. Girault, *Chem. Sci.*, 2015, **6**, 2705–2720.
45 K. Ge, H. Shao, E. Raymundo-Piñero, P. L. Taberna and P. Simon, *Nat. Commun.*, 2024, **15**, 1–10.
46 P. Brack, S. Dann, K. G. U. Wijayantha, P. Adcock and S. Foster, *JoVE)*, 2016, **114**, e54383.